Regular Article

Fabrication of Ru-doped CuMnBP micro cluster electrocatalyst with high efficiency and stability for electrochemical water splitting application at the industrial-level current density

Shusen Lin, Rutuja Mandavkar, Md Ahasan Habib, Sumiya Akter Dristy, Mehedi Hasan Joni, Jae-Hun Jeong [*], Jihoon Lee [*]

Department of Electronic Engineering, College of Electronics and Information, Kwangwoon University, Nowon-gu Seoul, 01897, South Korea

GRAPHICAL ABSTRACT

A novel dual-function Ru/CuMnBP micro particle electrocatalyst is successfully fabricated via hydrothermal reaction and Ru soaking approaches for overall water splitting application, which exhibits a low cell voltage of 3.13 V at an industrial level current density of 2000 mA/cm^2 in 1M KOH. The designed hybrid Pt/C|| Ru/CuMnBP shows higher catalytic behavior, requiring a lower bias of 2.64 V to maintain the current density of 2000 mA/cm^2.
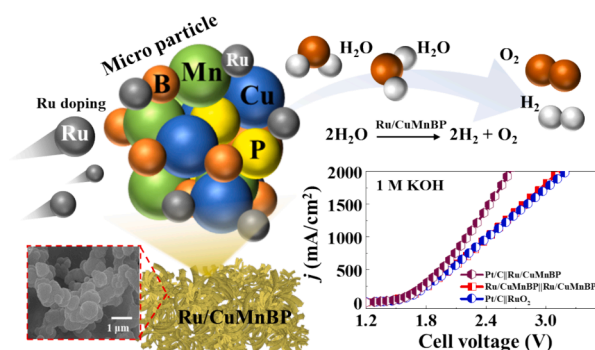
ARTICLE INFO

ABSTRACT

Electrochemical water splitting has been considered as a key pathway to generate environmentally friendly green hydrogen energy and it is essential to design highly efficient electrocatalysts at affordable cost to facilitate the redox reactions of hydrogen evolution reaction (HER) and oxygen evolution reaction (OER). In this work, a novel micro-clustered Ru/CuMnBP electrocatalyst is introduced, prepared via hydrothermal deposition and soaking-assisted Ru doping approaches on Ni foam substrate. Ru/CuMnBP micro-clusters exhibit relatively low HER/OER turnover overpotentials of 11 mV and 85 mV at 10 mA/cm^2 in 1 M KOH. It also demonstrates a low 2-E turnover cell voltage of 1.53 V at 10 mA/cm^2 for the overall water-splitting, which is comparable with the benchmark electrodes of Pt/C||RuO$_2$. At a super high-current density of 2000 mA/cm^2, the dual functional Ru/CuMnBP demonstrates an exceptionally low 2-E cell voltage of 3.13 V and also exhibits superior stability for over 10 h in 1 M KOH. Excellent electrochemical performances originate from the large electrochemical active surface area with the micro cluster morphology, high intrinsic activity of CuMnBP micro-clusters optimized through component ratio adjustment and the beneficial Ru doping effect, which enhances active site density, conductivity

and stability. The usage of Ru in small quantities via the simple soaking doping approach significantly improves electrochemical reaction rates for both HER and OER, making Ru/CuMnBP micro-clusters promising candidates for advanced electrocatalytic applications.

1. Introduction

Climate and environmental issues have led to a growing demand for renewable and green energy resources and hydrogen is considered as a potential energy alternative due to its advantages such as high energy density, zero-carbon emission and easy storage-transportation, etc. [1–5]. Hydrogen can be categorized in grey, blue, brown and green, etc. depending on the generation approaches. Electrochemical water splitting is a promising approach to generating green hydrogen with zero-carbon emission, which involves two heterogeneous electrochemical reactions of hydrogen evolution reaction (HER) and oxygen evolution reaction (OER), namely water splitting. Traditionally, noble-metal-based electrodes such as Pt/IrO$_2$ and RuO$_2$ exhibit excellent HER and OER performances but their scarcity and high cost hinder the industrial-scale application. At the same time, industry-relevant conditions such as high current density (HCD) and extended operational periods are economically crucial. HCD operation can ensure high-rate hydrogen production and economic advantages [6]. However, the extreme conditions associated with high bias can challenge the catalytic stability of electrocatalysts [6]. Thus, developing high-performance electrocatalysts that can operate under the HCD with high catalytic stability at affordable cost is of great importance for large-scale green-hydrogen implementation.

In the last decades, numerous efforts have been devoted to the design of electrocatalysts with the earth-abundant transition metals (TMs), i.e., Fe, Ni, Co, Cu, W, Mn, etc. such as TM-based carbides, nitrides, oxides, phosphides [5,7,8]. Nowadays, the combination of multiple metallic TMs with non-metallics is getting more research interest in designing high-performance electrocatalysts. The advantage of each element might be adapted to proper combination and condition. For example, the Cu oxidation states of 0, +1 and +2 can exhibit remarkable activity in the OER whereas low ionic conductivity for hydrogen protons can limit the HER kinetics [9,10]. On the other hand, the reversible cycling between the Mn^{2+}, Mn^{3+}, and Mn^{4+} oxidation states can demonstrate stable surface adsorption/desorption of H protons, which can be advantageous for HER activity [11,12]. Thus, putting Cu and Mn together in an electrocatalyst can be a viable choice. Cu can offer excellent corrosion resistance, earth-abundance, outstanding electrical and thermal conductivity and favorable electronic properties [13,14]. Mn is an economical and environment-friendly metal that can demonstrate high catalytic activity in alkaline electrolytes. In terms of non-metallic components, phosphorus (P) and boron (B) together can be worthwhile choices. In the integration of phosphorus with the TM, the P atoms can act as H proton and hydride acceptors, which is favorable for HER reaction [15]. For instance, the NiCuP catalyst exhibited excellent HER reaction and the NiCuP functioned as fast electron conductive channels with the higher conductivity of metal phosphides as compared with that of metal oxides [16,17]. Boron can supply electrons to the metallic sites, leading to the electron-enriched metal surface, which is beneficial for OER [18]. Also, the stability and surface conductivity can be largely improved since the TM-B can prevent excessive oxidation [19]. At the same time, hetero-atom doping (HAD) can be another route to improve the catalytic performance of electrocatalysts. HAD can offer added active sites, and improved intrinsic activity [20]. Meantime, some reported that poly-crystallization or amorphization can improve the active sites and stability of electrocatalysts as compared with the crystal counterparts [21,22]. HAD is a process of incorporating additional atoms into an already existing crystal matrix and thus poly-crystallization can occur inevitably, and this might bring improved active sites and stability through the doping process. Ru is known as a

top OER electrocatalyst due to the existence of Ru—O moieties and the Ru—H bond is similar to the Pt—H bond, indicating strong HER activity as well [20,23–26]. Through the HAD of Ru, only a fractional amount of Ru is necessary as compared with the pure Ru electrocatalysts. In this regard, doping a small amount of Ru into the CuMnBP matrix can be a promising way to further enhance the electrical conductivity and improve the intrinsic activity. In short, the combination of Cu, Mn, B and P and Ru-doping can be a rational route to fabricate highly effective electrocatalysts to improve both the HER and OER.

Herein, the Ru-doped CuMnBP electrode, namely Ru/CuMnBP, has been successfully fabricated as a bifunctional electrocatalyst for efficient overall water-splitting application. Various parameters such as reaction time, temperature and concentrations were thoroughly investigated. In addition, post-annealing is adapted at different stages to improve the overall crystallinity of electrocatalysts. The micro-clustered Ru/CuMnBP electrode exhibits excellent HER/OER activity and comparable or even better performances over the benchmark electrodes of Pt/C and RuO$_2$. Very low turnover HER/OER overpotentials and 2-E cell voltage are clearly demonstrated by the Ru/CuMnBP. In addition, excellent HCD characteristics are observed under very high current operation and superior electrode stability is observed with the Ru/CuMnBP. Systematic precursor optimization can largely maximize the catalytic advantages of each element and Ru doping can further improve the intrinsic activity of electrocatalysts by increasing active sites and conductivity. Also, the micro-cluster topology can offer a large surface area that ensures sufficient contact between the electrode and electrolyte. Overall, the Ru/CuMnBP micro-clusters have a high potential in realistic industrial applications.

2. Experimental section

2.1. Source materials and precursor preparation

The precursor solution containing copper (II) sulfate (CuSO$_4$·5H$_2$O, $\geq$ 98.0 %), manganese (II) sulfate (MnSO$_4$·H$_2$O, $\geq$ 98.0 %), sodium hypophosphite (H$_2$NaPO$_2$·H$_2$O, $\geq$ 99.0 %), boric acid (H$_3$BO$_3$, $\geq$ 99.5 %) and urea (CH$_4$N$_2$O, $\geq$ 99.0 %) dissolved in 30 mL DI water was used for the fabrication of CuMnBP electrode. All the chemicals were purchased from Sigma-Aldrich (USA) and were used as received without further purification. Details regarding the molarity used and concentration optimization are provided in the corresponding section. Ruthenium (III) chloride (RuCl$_3$·H$_2$O, $\geq$ 99.98 %) was dissolved in 30 mL DI water to make a homogeneous Ru precursor for the doping process. The molarity of Ru was specified in the corresponding section.

2.2. Fabrication of Ru/CuMnBP electrode

CuMnBP electrodes were firstly fabricated by a hydrothermal deposition, with systematic optimization of reaction parameters and precursor configuration. The hydrothermal reaction duration changed from 2, 4, 8, 12 to 16 hrs at a fixed temperature of 100 °C and then the temperature was varied from 100 to 160 °C with intervals of 20 °C. Subsequently, the precursor configuration was optimized by varying the molarity ratio of B-P and Cu-Mn. After that, the post-annealing treatment was conducted and optimized to enhance electrode performance. The annealing duration was varied at intervals of 2, 4, 8, 12, and 16 h, while the temperature was set at 100, 200, 300, and 500 °C. The temperature rising rate was 4 °C/s during the vacuum annealing process. The surface morphology, catalytic activities and corresponding discussion along with the changed parameters can be found in Fig. S7 – S18

and supplementary S-1.2. The optimal CuMnBP electrode was achieved under the following conditions: synthesis at 120 °C for 4 h, using a precursor solution containing 6 mmol B, 6 mmol P, 1.8 mmol Cu, 0.2 mmol Mn, and 10 mmol urea, followed by annealing at 300 °C for 10 min. The concentration of Ru dopant, soaking time and temperature were optimized and specified in the corresponding section. The schematic of the synthesis process is displayed in Fig. S2.

2.3. Physical and optical characterization

The surface morphological and elemental analysis were performed by using a scanning electron microscope (SEM, Regulus 8230 Hitachi, Japan) and energy-dispersive X-ray spectrometer (EDS, Ultimax, Oxford Instruments United Kingdom) instruments. The Raman measurement was done in NOST system (Nostoptiks, South Korea) integrated with a 532 nm laser, spectrograph (ANDOR SR-500, United Kingdom), charge-coupled device (CCD) and various optics. The crystallographic nature and diffraction planes were examined by X-ray diffraction (XRD, D8 Advance, Bruker, USA) at a scanning rate of 2°/min by the Cu Kα radiation ($\lambda = 1.5406$ Å). The element composition and chemical state were analyzed by utilizing X-ray photoelectron spectroscopy (XPS) at 1.5 KV under $< 10^{-8}$ torr with the X-ray spot size of 10 μm (FC-XP10, Thermo Fisher Scientific, USA).

2.4. Electrochemical characterization

3-electrode (3-E) electrochemical measurements were performed by using a standard Wizmac workstation system (Wizmac, South Korea) in which the Ru/CuMnBP electrode was employed as a working electrode, Ag/AgCl as reference electrode and Platinum as contour electrode respectively. The linear scanning voltammetry (LSV) curves were measured by applying the potential ranging from −0.6 V to 0.2 V vs. RHE and 1.2 V to 2.0 V vs. RHE for HER and OER respectively with a sweeping rate of 5 mV/s. The polarization curves were plotted as received without an iR correction. The electrochemical impedance spectroscopy (EIS) measurements were performed in the frequency range of 100 kHz to 0.1 Hz at 10 mA/cm^2 with an amplitude of 5 mV. The cyclic voltammetry (CV) was recorded at various scan speeds between 40 and 180 mV/s in the non-faradic potential range of 0.2–0.3 V vs. RHE for the HER and 1.04–1.14 V vs. RHE for the OER.

3. Result and discussion

3.1. Optimization and structure characterization of Ru/CuMnBP electrode

In this work, the Ru-doped CuMnBP, namely Ru/CuMnBP micro clusters electrode was fabricated for overall water splitting application. The based CuMnBP electrode was synthesized on bare nickel foam (NF) using a hydrothermal approach. To maximize the intrinsic activity of Cu, Mn, B and P and to improve the efficiency of the electrode, the fabrication parameters have been systematically optimized such as hydrothermal deposition condition (duration and temperature), Cu-Mn concentration, B-P concentration and post-annealing treatment as shown in Figs. S7–S18. The details have been discussed in supplementary S-1.2. As a result, the precursor mixture containing 1.8 mmol of CuSO$_4$, 0.2 mmol of MnSO$_4$, 6 mmol of NaH$_2$PO$_2$ and H$_3$BO$_3$ and 10 mmol of NH$_2$CONH$_2$ was identified to reach the highest HER/OER activity. Here, Cu-based electrodes generally exhibited superior electrical conductivity and stability and their multiple oxidation states are particularly effective for the adsorption and desorption of electrolyte ions during the redox reaction [13]. Similarly, Mn's reversible cycling among their oxidation states is favorable for OER reaction and its low electrical conductivity can be compensated by the incorporation of Cu element [27]. As for boron (B), owing to its distinctive electronic properties of forming strong chemical bonds with itself and with metal

atoms, it can serve as a bridge among the deposited atoms [19]. P-containing materials exhibited fast carrier mobility and strong electronegativity, which can significantly boost the absorption of positively charged protons (H$^+$) [28,29]. Here, the incorporation of B and P can also improve the limited ionic conductivity in Cu and Mn via the kinetic electron transfer. The vacuum annealing process is used to further enhance the quality of local crystallinity [28,29].

Subsequently, Ru heteroatom was doped into CuMnBP matrix using a simple soaking approach to enhance the intrinsic activity. The doping temperature was firstly varied as seen in Fig. S19–S22. SEM images revealed that the pronounced micro-cluster structure remained stable at room temperature. Nevertheless, surface agglomeration started to appear when the doping temperature exceeded over 100 °C, primarily due to the surface adatom diffusion initiated by thermal energy. The change in surface morphology indicates the decreased active surface area, which negatively affects catalytic activity. The EDS spectra and HER/OER activity for this set are provided in Fig. S19–S22. The doping duration was then varied from 5 to 20 mins as seen in Fig. S23–S26. The microcluster was stably maintained on the nickel foam as shown in Fig. S23. The EDS spectra are provided in Fig. S24–S25. The best HER/OER results were obtained at 10 mins as seen in Fig. S26.

Fig. 1 shows the surface characterization of Ru/CuMnBP electrodes for the Ru dopant concentration variation set. Despite the increased molarity of Ru, there was no obvious change in surface morphology as seen in Fig. 1a-d. The EDS spectrum for the 1 mg sample is shown in Fig. 1e, revealing the coexistence of Ru, Cu, Mn, B and P elements. The EDS phase maps for single particles are shown in Fig. 1(f–f-5), indicating that Ru dopant was uniformly loaded on the CuMnBP matrix. The corresponding line profiles in Fig. 1(g-1–g-5) clearly shows the elemental distribution across micro cluster structure. The weight percentage indicated that only a small fraction amount of Ru was used here. The large-scale SEM images and EDS spectra are provided in Fig. S27–S29.

The Raman spectra for this set are shown in Fig. 2a, where several characteristic peaks were observed at 467, 604, 995 and 1061 cm^{-1}. The Raman band at 467 cm^{-1} is similar to the Mn—O bond [30]. The peak at 603 cm^{-1} can be related to the Cu—O bonds due to the existence of CuO and Cu(OH)$_2$ [13]. The Raman peaks at 995 and 1061 cm^{-1} can correspond to antisymmetric stretching vibrations of the phosphate [PO$_4$]$^{3-}$ ligands and the peak centered at 1035 cm^{-1} might correspond to active oxygen species (O—O) [31–33]. Here, the 1 mg Ru sample demonstrated the highest peak intensity, indicating high-quality crystallinity. However, along with the increased molarity of Ru, the peak intensity gradually decreased. The trend in peak intensity changes for 995 and 1061 cm^{-1} can be found in the corresponding contour plots in Fig. 2(a-1–a-2). The degradation can be mainly due to the increased density of spatial arrangements during the heteroatom doping, which can increase the possibility of a disorder in surface crystallinity [34]. X-ray diffraction (XRD) was employed to examine the polycrystalline structure of the Ru/CuMnBP electrode as shown in Fig. 2b. The two main diffraction peaks at 44.12° and 51.40° correspond to the (1 1 1) and (2 0 0) planes of bare nickel foam substrate [35]. Additionally, several small peaks at 26.93, 31.80, 33.06, 34.99, 59.28 and 61.25° were observed together with multiple secondary peaks throughout the spectrum. However, after comparing with ICCD/JCPDS database, there are no exactly matched XRD patterns as seen in Figs. S39–S40. This indicated that the crystalline orientation was randomly distributed on the surface of the electrode, resulting in mixed phases due to the polycrystalline nature of the Ru/CuMnBP electrode [36]. It is worth mentioning that the polycrystalline nature of the electrode could accelerate the reaction kinetics by enhancing the electron density [37,38]. Also, more active sites can be exposed as compared to the surface in the single crystal phase. On the other hand, Ru heteroatom doping can generate more surface regions that are oriented in different directions. Such increased grain boundaries in polycrystalline structures demonstrate enhanced stability since multiple grains can distribute stress and strain more effectively [39]. A more details discussion of XRD can be found in the supplementary S-1.7.
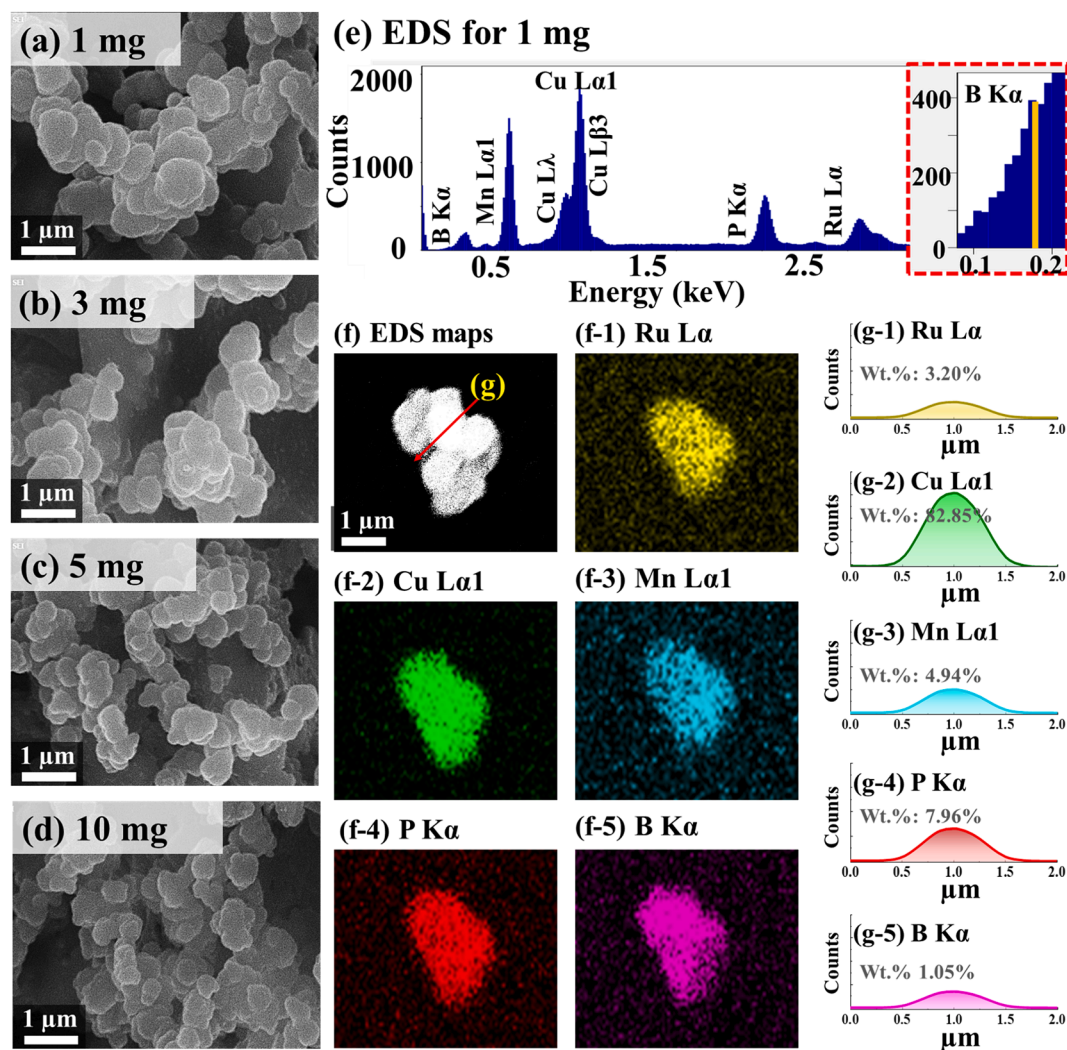
Fig. 1. Ru/CuMnBP electrodes with Ru dopant concentration variation. (a–d) SEM images of Ru/CuMnBP electrodes. (e) EDS spectrum of 1 mg Ru/CuMnBP electrode. (f–f-5) EDS phase maps of Ru Lα, Cu Lα1, Mn Lα1, P Kα and B Kα. (g–g-5) EDS line profiles.

To probe the surface elemental composition and valance states of Ru/CuMnBP electrode, an X-ray photoelectron spectroscopy (XPS) was performed as shown in Fig. 2(c–c-5). The full spectrum in Fig. 2c confirms the co-existence of Ru, Cu, Mn, B and P elements. In the high-resolution Ru 3d spectrum in Fig. 2(c-1), three peaks were observed, located at 279.6, 285.4 and 284.8 eV. The peaks at 284.8 and 279.6 eV can be assigned to the Ru $3d_{3/2}$ and $3d_{5/2}$ and the peak centered at 285.4 eV corresponds to the C—C bond [40]. As compared to the pristine Ru $3d_{3/2}$ and $3d_{5/2}$ peaks at 280.1 and 284.27 eV according to the XPS handbook, the negative shift was observed, indicating the increased electron density in the vicinity of Ru atoms [41]. Here, the binding energy (BE) shift in Ru is probably due to the lattice strain and local electronic redistribution [42]. For Cu 2p spectrum in Fig. 2(c-2), the peaks at 933.61 and 953.34 eV correspond to Cu^+ $2p_{3/2}$ and $2p_{1/2}$, indicating the formation of Cu_2O [43]. The BEs of 935.68 and 954.58 eV are related to Cu^{2+} $2p_{3/2}$ and $2p_{1/2}$, suggesting the existence of CuO on the surface [43,44]. The shake-up satellite peaks were found at 942.43 and 962.0 eV [43]. The pristine Cu $2p_{3/2}$ and $2p_{1/2}$ peaks are located at 933.4 and 953.3 eV and here positive shift was demonstrated for both, indicating the electron donating process and the strong electronic interaction [43]. In Mn 2p spectrum, the BE values of 640.5 and 650.2 eV corresponding to MnO and peaks at 642.4 and 652.8 eV indicated the presence of MnO_2 [44]. As compared to its pristine peaks of Mn $2p_{3/2}$ and $2p_{1/2}$ (639.0 and 650.05 eV), the deconvoluted peaks exhibited a slightly positive shift, meaning the kinetic electron transfer process from Mn to other elements. In P 2p spectrum, P $2p_{3/2}$ and $2p_{1/2}$ peaks were found at 129.17 and 130.0 eV, which exhibited negative shifts of 0.73 and 0.74 eV from its pristine positions (129.9 and 130.74 eV) respectively. BE shifting towards lower energy indicated more electron occupation near P atoms [42]. The deconvoluted peaks centered at 131.03 and 136.93 eV correspond to $(PO_4)^{3-}$ and P_2O_5 respectively [45]. Here, P has various oxidation states and its valence can change from P^{3+} to P^{x+} (x < 5). The BEs of its intermediate oxides are generally located from 131 to 136 eV [46]. The B 1s spectrum in Fig. 2(c-5) exhibits two distinct peaks at 190.7 and 186.8 eV, which are assigned to the B_2O_3 oxidation states and B^0 elemental state [47]. The B 1s level exhibited a negative shift of 2.6 eV from its initial position (189.4 eV), indicating increased electron density and orbital hybridization with other elements.[47] With regard to O 1s spectrum as seen in Fig. S56a, three peaks were observed, located at 535.7, 534.0 and 531.5 eV, which were assigned to absorbed H_2O, M—OH and M—O bonds (M = Ru, Cu and Mn) [48]. The pristine O 1s peak is found at 531.0 eV and here the negative shift indicates gaining electrons to form metal-oxide bond [48]. Overall, the kinetic electron transfer process among Cu, Mn, B and P indicated the strong bond chemical bond formation and the addition of Ru heteroatom demonstrated the ability to modulate the electronic structure of CuMnBP matrix. Additional XPS discussions are provided in supplementary S-1.8.
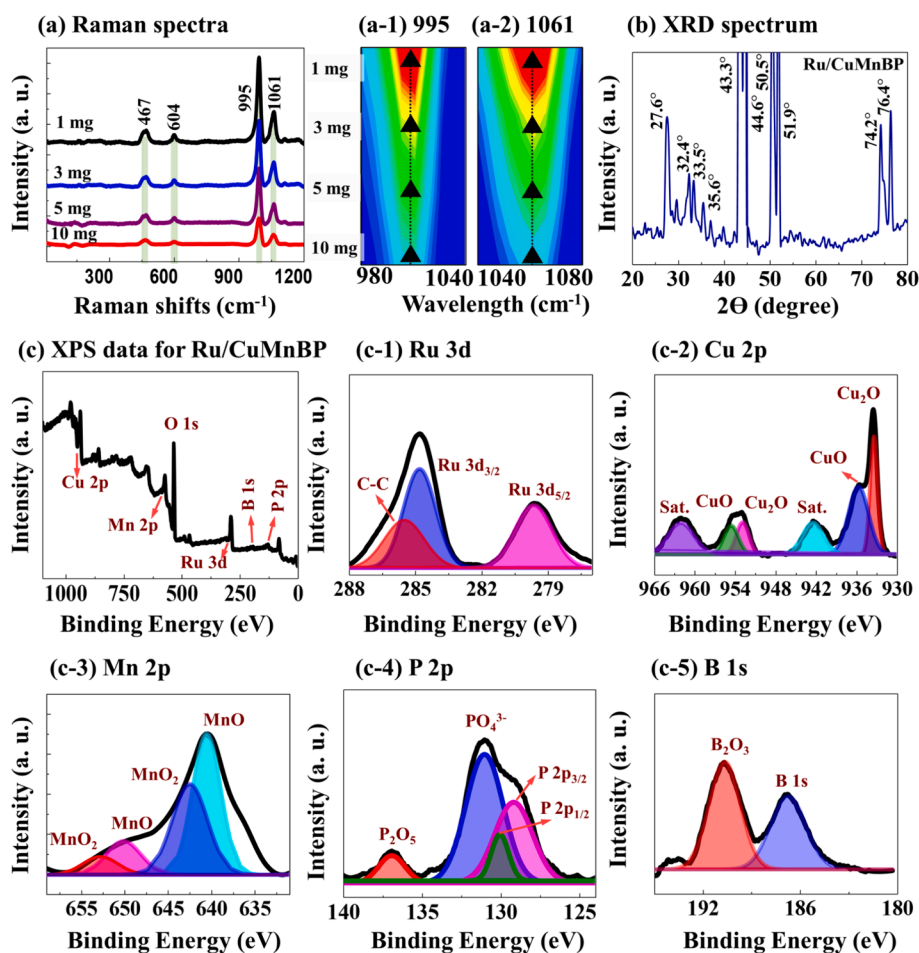
Fig. 2. Structural analyses on the Ru/CuMnBP electrode. (a) Raman spectra of Ru/CuMnBP in Ru concentration variation set. (a-1–a-2) Corresponding Raman contour plots at 995 and 1061 cm^{-1}. (b) X-ray diffraction (XRD) pattern. (c) X-ray photoelectron spectroscopy (XPS) full scan of Ru/CuMnBP. (c-1–c-5) Zoom-in XPS spectra of Ru 3d, Cu2p, Mn 2p, P 2p and B 1s.

3.2. Electrochemical characterization of Ru/CuMnBP electrode

Fig. 3 shows the electrochemical performance of Ru/CuMnBP electrodes in a 3-electrode (3-E) setup, with varying molarities of Ru in 1 M KOH. The HER/OER linear sweep voltammetry (LSV) results are presented in Fig. 3a and Fig. 3e. Both HER and OER activity followed the order of 1 mg > 3 mg > 5 mg > 10 mg. The 1 mg sample exhibited the lowest overpotential values of 67 and 346 mV at the current density of 100 mA/cm^2 for HER/OER respectively. This superior performance of the 1 mg sample can be attributed to its highest surface crystallinity, which is crucial for efficient charge transfer and transport. Additionally, the balance between the trap states and extra active sites is imperative and here I mg was proved to be the optimal molarity for maximizing the intrinsic activity. The specific values at 50 and 100 mA/cm^2 are shown in Fig. 3(a-1) and Fig. 3(e-1). In terms of gas generation mechanism, the HER reaction in an alkaline medium can be described as the Volmer and Heyrovsky steps, in which the active sites of the metal can react with the water molecule. M+H$_2$O → M-H* + OH (Volmer step), M-H* + H$_2$O+e$^-$ → M+OH$-$ + H$_2$ (Heyrovsky step). At the same time, the high coverage of M-H species tends to combine, indicating the Tafel step (2 M-H* → 2 M+H$_2$) [10,49]. The alkaline OER reaction pathway can be summarized by the following steps[10,49]: OH$^-$ + M = M-OH+e$^-$, M-OH+OH$^-$ = M-O+H$_2$O+e$^-$, 2 M-O→2M+O$_2$. Another reaction route can also occur M-O+OH$^-$ = M-OOH+e$^-$; M-OOH+OH$^-$ → O$_2$ + H$_2$O+e$^-$ + M. M represents the metallic active sites (Cu, Mn and Ru). On the other hand, the oxidation peaks were commonly observed in all OER results, mainly due to the oxidation state transformation of Co^0/Cu^{III} and Mn(II)/Mn(IV)

[10,49]. The full scan CV measurement and detailed discussion are provided in Fig. S41 and supplementary S-1.5. Further, to get detailed insights into HER and OER kinetics, the Tafel slopes were studied as shown in Fig. 3(a-2) and Fig. 3(e-2). The 1 mg electrode shows the smallest Tafel slope of 59 and 186 mV/dec for HER/OER as compared to other electrodes, indicating the highest reaction rate and improved charge transfer characteristics. The Tafel slope of HER is located in between the well-known Tafel slopes of 40 and 120 mV/dec, meaning that the reactions are dominated by the Heyrovsky step. For OER, the slope value over 120 mV/dec indicated that the rate-determining reactions may involve beyond simple electron transfer processes such as the formation of M-OH active sites or M-O species [50]. Electrochemical impedance spectroscopy (EIS) measurement was conducted to further probe the HER/OER kinetics as seen in Fig. 3b and Fig. 3f. The 1 mg electrode had the lowest charge transfer (R$_{ct}$) value of 23.62 Ω at 0.011 V for HER and 35.43 Ω at 1.31 V for OER respectively. These lower resistance values can be attributed to the improved conductivity and faster charge transferability between the surface of the electrode and electrolyte [51]. To assess the electrochemical active surface area (ECSA) of the electrode, the double layer capacitance (C$_{dl}$) was calculated as seen in Fig. 3c and Fig. 3g based on the CV measurement. The corresponding anodic and cathodic current density plots are shown in Figs. S30–S32. The highest C$_{dl}$ value was observed in the 1 mg electrode with the C$_{dl}$ of 8.9 and 7.5 mF/cm^2 for HER/OER, indicating the highest electrochemical active surface area. The ECSA was calculated to be 111.25 and 94.5 mF/cm^2 for HER and OER using the equation of ECSA = A × C$_{dl}$/C$_s$ [52]. A is the geometric surface area of Ru/CuMnBP. C$_s$
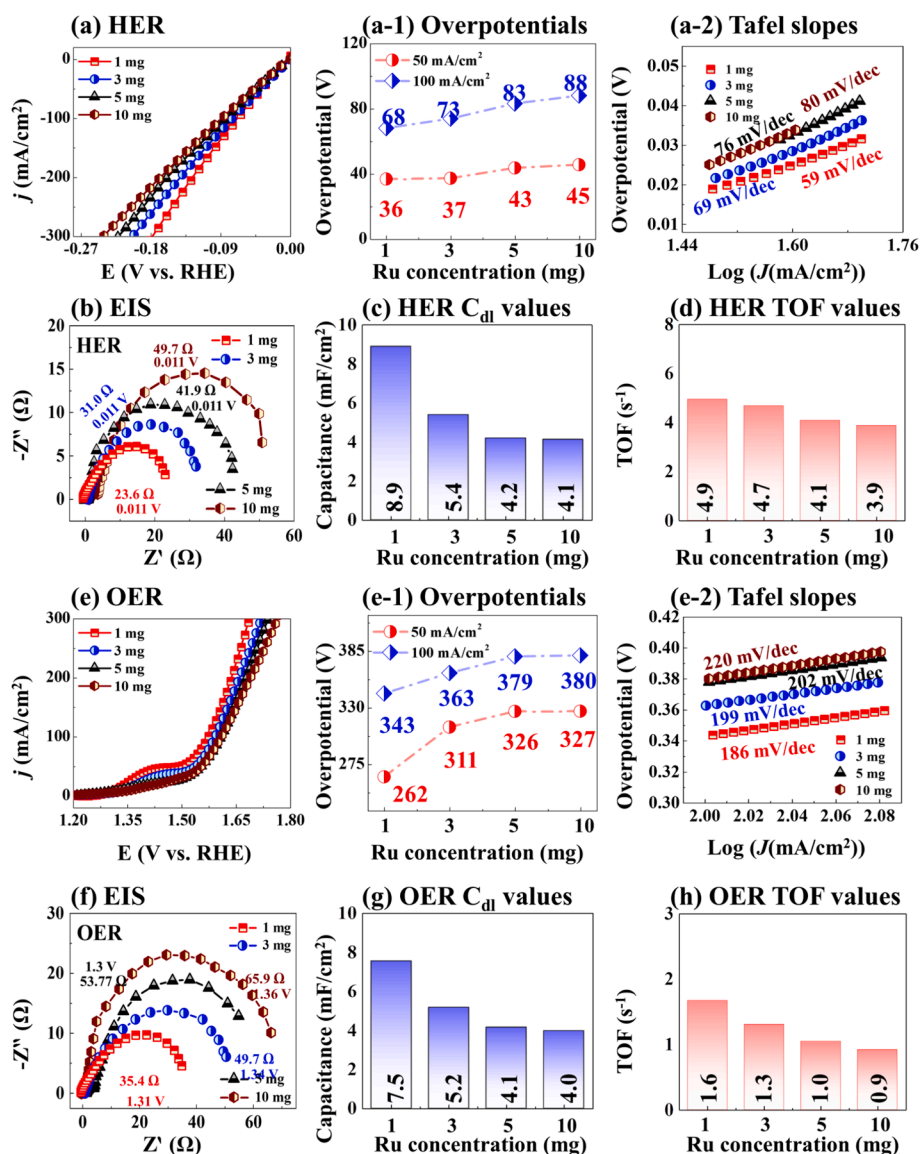
Fig. 3. 3-electrode (3-E) electrochemical analyses on the Ru doping concentration variation set in 1 M KOH. (a, e) HER/OER polarization curves. (a-1, e-1) Specific overpotentials at 50 and 100 mA/cm². (a-2, e-2) Tafel slopes. (b, f) Electrochemical impedance spectroscopy (EIS). (c, g) Double-layer capacitance (C_{dl}) values. (d,h) Turnover frequency (TOF) values.

represents the surface electronic double layer of the ideal smooth electrode, typically taken as 0.040 mF/cm² in an alkaline solution. Turnover frequency (TOF) values were calculated to assess the intrinsic activity of the Ru/CuMnBP electrode as seen in Fig. 3d and 3 h. Here, it was assumed that all the atoms were actively participating in the redox reaction. Similarly, the 1 mg sample demonstrated the lowest value of 4.9 and 1.6 site^{-1} s^{-1} for HER/OER, indicating improved catalytic activity. The detailed calculation and description were provided in supplementary S-1.6. The Ru doping effect on CuMnBP was also systematically investigated as seen in Fig. S33–S38 and the corresponding discussion is provided in supplementary S-1.10.

In addition, to determine the faradic efficiency (EF), the generated H_2 and O_2 from experimental results and theoretical calculations were compared. The experimentally generated H_2 and O_2 were collected by using the water–gas displacement method as seen in Fig. S42 and the CA measurement was conducted at 60 mA for a constant 30 min. The detailed calculations are provided in supplementary S-1.10. The specific values from experimental and theoretical calculation along with the time progression are shown in Fig. S43. Here, the Ru/CuMnBP electrode demonstrated 93.5 and 91.8 % efficiency respectively as seen in Fig. 4a.

Overall the optimized Ru/CuMnBP electrode exhibited improved HER/OER catalytic performance. The enlarged surface area, enhanced electrical conductivity and increased quality of crystallinity enabled a high rate of adsorption and desorption of hydride/oxyhydroxide intermediates. Also, the balance between Cu and Mn has maximized the intransitive activity and minimized the by-product generation. The B-P ratio adjustment further optimizes the absorption energy of active sites towards intermediates by altering the electronic structure of metals and forming metal-boride or metal-phosphide bonds. Moreover, as discussed in the XPS section, the kinetic electron transfer from B and P can lead to electron-enriched active sites, which are particularly good for catalytic reactions. Meanwhile, the Ru doping induced the formation of additional active sites and presented the modulated electronic structure, which is also critical for gas generation [52]. Fig. 4b-c shows the HER and OER performance comparison of the as-prepared best Ru/CuMnBP electrode. In Fig. 4b, it was found that the Ru/CuMnBP electrode demonstrated quite good HER activity, which ranks it as one of the best electrocatalysts among recent publications. The OER activity of Ru/CuMnBP is also comparable to other transition-metal-based electrodes as seen in Fig. 4c. The specific values are provided in Table 1 and S1.
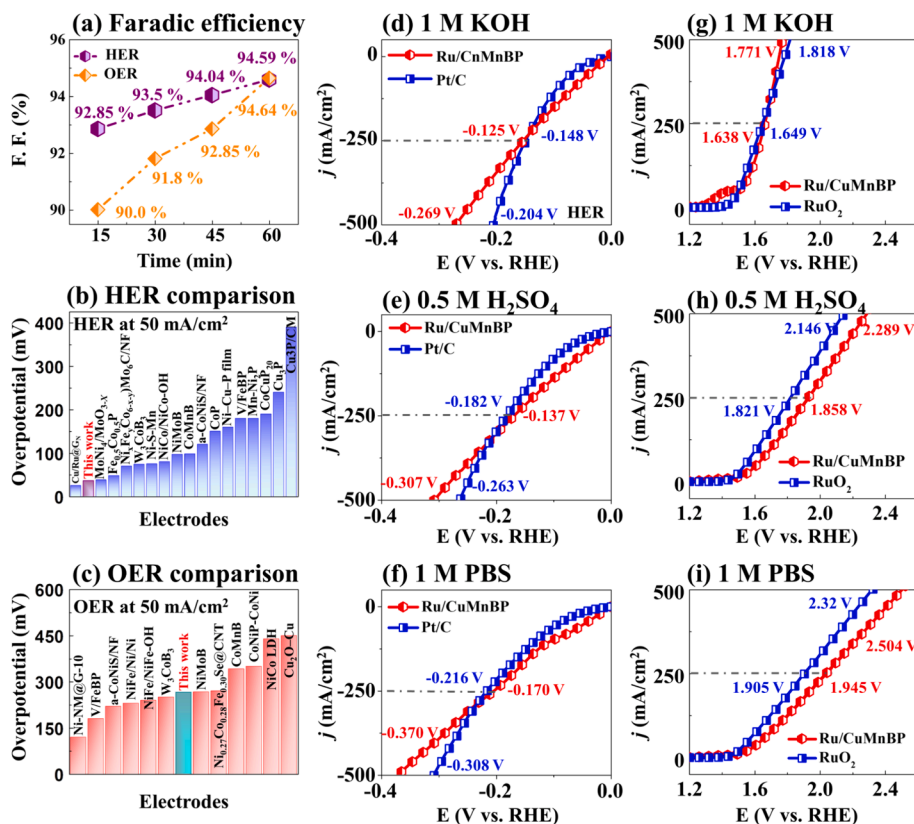
Fig. 4. 3-E electrochemical performances of the best Ru/CuMnBP electrode in different pH solutions as compared with the benchmark electrodes. (a) Faradic efficiency at different time intervals for HER and OER. (b, c) HER/OER performance comparison of the state of art electrodes at 50 mA/cm^2. (d–f) HER polarization curves in 1 M KOH, 0.5 M H$_2$SO$_4$ and 1 M PBS. (g–i) OER polarization curves.

Table 1
3-E HER performance comparison of transition metal-based electrodes at the current density of 10 and 50 mA/cm^2.

Electrocatalysts	Electrolyte Solution	Overpotential [mV] at 10 mA/cm^2	Overpotential [mV] at 50 mA/cm^2	Reference
Cu/Ru@G$_N$	1 M KOH	8	25	[63]
Ru/CuMnBP	**1 M KOH**	**11**	**36**	**This work**
MoNi$_4$/MoO$_{3-X}$	1 M KOH	17	38	[64]
Ni-S-Mn deposits	1 M KOH	20	75	[65]
W$_3$CoB$_3$	1 M KOH	21	74	[66]
Fe$_{0.5}$Co$_{0.5}$P nanowires	0.5 m H$_2$SO$_4$	37	48	[67]
NiMoB	1 M KOH	37	97	[38]
CoP	0.5 m H$_2$SO$_4$	67	150	[68]
CoMnB	1 M KOH	–	98	[69]
NiP$_{1.93}$Se$_{0.07}$	0.5 M H$_2$SO$_4$	102	–	[70]
Mn-Ni$_2$P	1 M NaOH	103	180	[71]
Ni–Cu–P film	1 M KOH	120	160	[72]
CoCuP	1 M KOH	138	190	[73]
Cu$_3$P NW array	0.5 m H$_2$SO$_4$	143	240	[74]
Cu3P/CM	1 M KOH	252	390	[75]

Further, the electrochemical performance of Ru/CuMnBP was tested in different pH media such as KOH, H$_2$SO$_4$ and neutral PBS solutions and was compared with benchmark Pt/C and RuO$_2$ electrodes as seen in Fig. 4d–i. The fabrication details of Pt/C and RuO$_2$ electrodes are provided in supplementary S-1.5 and the corresponding surface morphological, optical and electrochemical characterization are shown in

Fig. S5–S6. In alkaline media in Fig. 4d, the Ru/CuMnBP electrode demonstrated 36 mV overpotential at 50 mA/cm^2, while 63 mV is required for the Pt/C electrode to reach the same current density. For OER as seen in Fig. 4g, The catalytic activity of Ru/CuMnBP is comparable to the reference electrode with 266 mV at 50 mA/cm^2 as compared to the 270 mV in RuO$_2$. In an acidic solution, slight degradation appeared for HER at high current density for both Ru/CuMnBP and Pt/C with the overpotential values of 307 and 263 mV at 500 mA/cm^2 as seen in Fig. 4e. For OER in Fig. 4h, both electrodes also exhibited decreased activity with the overpotential values of 1059 and 916 mV reaching 500 mA/cm^2. As an oxidizing agent, it interacts with the metal or metalloid species on the surface and causes corrosion, which results in a decrease in performance [53]. In PBS solutions as seen in Fig. 4f and i, more degradation was observed here, which is mainly due to the poor conductivity, that limited the charger transfer process [54]. As compared to bare Ni foam as seen in Fig. S44, the Ru/CuMnBP electrode demonstrated large enhancement, indicating superior high intrinsic activity. Further, the steady-state response in KOH solution was conducted for both HER at 0.01, 0.03, 0.06 and 0.12 V and OER at 1.31, 1.57, 1.63 and 1.68 V for ~ 30 min as shown in Fig. S45. The CA output was stably maintained at a certain current density and after comparing the values obtained from LSV curves, there were neglectable changes without exceeding 1.44 % and 2.52 % for both HER and OER respectively [55]. The repeatability test was performed via testing the HER/OERr results after 1000 cycles CV measurement as seen in Fig. S46. The obtained results are almost similar to the initial value.

Based on the above results, the 2-electrode (2-E) activities of Ru/CuMnBP in different pH media were examined and summarized in Fig. S47 by taking Ru/CuMnBP electrodes as both anodic and cathode, namely Ru/CuMnBP || Ru/CuMnBP. The LSV results show that the cell voltages of 2.03, 2.59 and 2.84 V were required at 500 mA/cm^2 in alkaline, acidic and neutral media respectively. Especially, in the KOH

solution, Ru/CuMnBP demonstrated comparable performance to the benchmark system. Given the high rate of production generation and economic advantages, the decent catalytic activity at current density (>500 mA/cm^2) is critical for industrial application [6]. Hence, the electrochemical performance at a high current density of 2000 mA/cm^2 was tested as seen in Fig. 5. In Fig. 5a, the Ru/CuMnBP demonstrated a better result at 2000 mA/cm^2 with the cell voltage of 3.13 V as compared to the benchmark system of 3.21 V. Further, the Ru/CuMnBP || Ru/CuMnBP system was tested in 6 M KOH solution as seen in Fig. 5b. A lower voltage of 2.85 V was required to maintain the same current density, which is mainly due to the increased concentration of K$^+$ and OH$^-$ ions. The long-term stability is another critical factor in evaluating electrocatalysts and here 120 h-continuous operation was conducted in harsh industrial conditions (6 M KOH @ 60 °C) as seen in Fig. 5c. The output was stably maintained at a constant value of 2.86 V without too much fluctuation, which is similar to the value extracted from the LSV results. The CA response at different voltages is provided in Fig. S48, where the results obtained from CA output matched well with that from LSV curves. The repeatability test in Fig. S49 exhibited minor changes after 1000 cycles of redox redox reactions. The 2-E performance was carried out in the natural seawater (SW) and river water (RW) with and without KOH for further study as shown in Fig. S50 and Fig. 5d. In RW as seen in Fig. S50a, both systems exhibited quite low activity here, which was mainly due to the lack of conductive ions in RW [42]. After the addition of KOH into RW, 2.21 and 1.90 V at 100 mA/cm^2 were required for Ru/CuMnBP and benchmark electrode respectively. In SW in Fig. S50b, 4.66 and 5.61 V were needed to catalyze the 800 mA/cm^2 and in SW+1 M KOH, 6.00 and 6.18 V were required to maintain 1500 mA/cm^2. Natural water may contain dissolved salts, particulates, various chemical compounds, and interfering anions like chlorides thus reduced performance was observed for river water.[56] despite the existence of

contains and impurities, the induced K$^\pm$ and OH$^-$ can effectively improve the ionic conductivity of the solution [57].

By taking advantage of OER results of Ru/CuMnBP, a hybrid system configured by Ru/CuMnPB, Pt/C||RuO$_2$ was proposed. The electrochemical activity in 1 and 6 M KOH solution are shown in Fig. 5(e–f). Here it was found that there is a huge increase in both experimental and industrial conditions with the cell voltage of 2.64 and 2.54 V to maintain the 2000 mA/cm^2. Such high activity is suitable for industrial applications, indicating that the Ru/CuMnBP electrode is promising in replacing the traditional RuO$_2$ electrode. Furthermore, the long-term stability of 12 hrs was performed as shown in Fig. 5g, revealing superior stability without significant fluctuation in output. The electrochemical performances of the hybrid system in different pH media are provided in Fig. S51. CA response and stability test are provided in Figs. S52–S53, which all confirmed the superior stability of the hybrid system. Here the slight fluctuations in CA curves at 1500 and 2000 mA/cm^2 can be due to the high-rate bubble generation and high polarization environment. The SW+KOH examination of the hybrid system in Fig. 5h demonstrated a better catalytic activity of 5.27 V at 1500 mA/cm^2 than others. The performances in pure SW and RW+KOH are provided in Fig. S54. Overall, the electrochemical properties of Ru/CuMnBP electrode are summarized in Tables S2 – S4. The comparison of two-electrode performance with other transition metal-based electrodes at 50 mA/cm^2 in 1 M KOH is provided in Fig. 5i and the corresponding specific values are summarized in Table 2.

3.3. Characterization after stability test

Fig. 6 shows the morphological and optical analysis of Ru/CuMnBP electrode following the stability test. The SEM image of the fresh electrode in Fig. 6a shows the micro-clusters approximately 1 μm in width
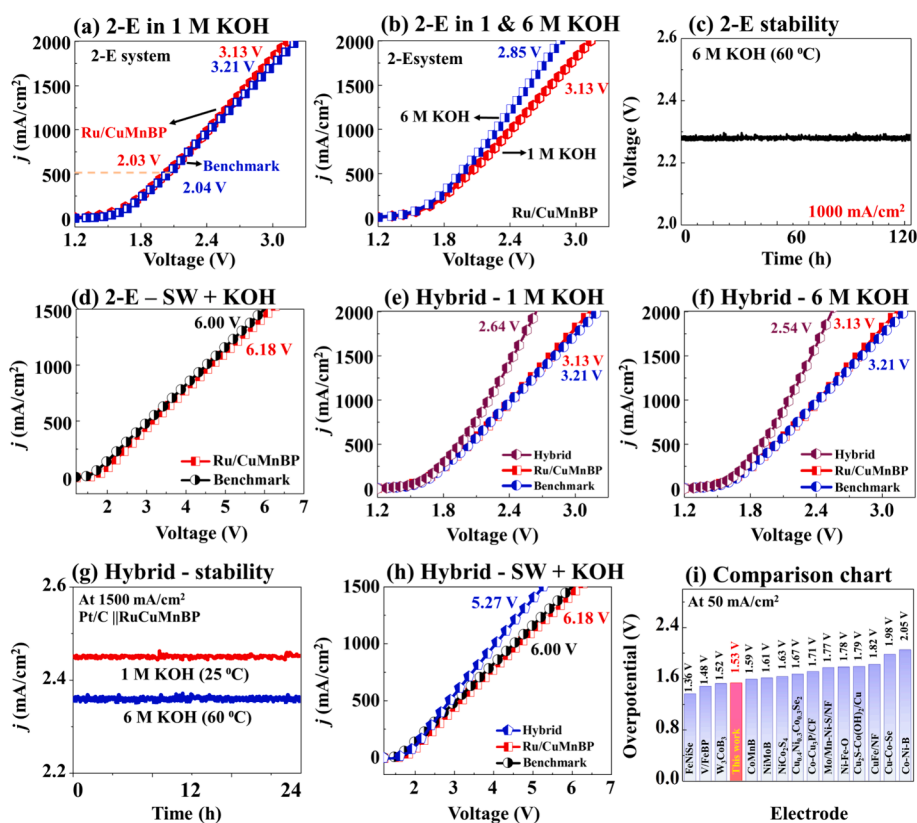

Fig. 5. 2-E performance of Ru/CuMnBP MPs, Hybrid and benchmark in different KOH and natural water. (a) Bi-functional performances of Ru/CuMnBP in 1 M KOH at high current density. (b) Comparison of high-current LSV in 1 M (25 °C) and 6 M (60 °C) KOH. (c) Stability performance in 6 M KOH at 60 °C for 120 h. (d) 2-E performance in seawater (SW) + KOH. (e) 2-E performance of hybrid, Ru/CuMnBP and benchmark configuration in 1 M KO. (f) 2-E performance for hybrid in 1 M (25 °C) and 6 M (60 °C) KOH. (g) Stability test at 1500 mA/cm^2 for hybrid configuration. (h) LSV curves in SW+KOH. (i) 2-E performance comparison.

Table 2

Comparison of 2-electrode overall water splitting performance of transition metal-based electrode at the current density of 50 mA/cm^2.

Electrocatalysts	Electrolyte Solution	Overpotential [V] at 50 mA/cm^2	Reference
FeNiSe	1 M KOH	1.36	[76]
W$_3$CoB$_3$	1 M KOH	1.52	[66]
Ru/CuMnBP	**1 M KOH**	**1.53**	**This work**
NiMoB	1 M KOH	1.61	[38]
NiCo$_2$S$_4$	1 M KOH	1.63	[77]
Cu$_{0.4}$Ni$_{0.3}$ −Co$_{0.3}$Se$_2$	1 M KOH	1.67	[78]
CoMnB	1 M KOH	1.68	[69]
Co-Cu$_3$P/CF	1 M KOH	1.71	[79]
Mo/Mn-Ni-S/NF	1 M KOH	1.77	[80]
Ni-Fe-O	1 M KOH	1.78	[81]
Cu$_2$S-Co(OH)$_2$/Cu	1 M KOH	1.79	[82]
CuFe/NF	1 M KOH	1.82	[83]
Cu-Co-Se	1 M KOH	1.98	[84]
Co-Ni-B	1 M KOH	2.05	[85]

while a rougher surface is observed post-stability in Fig. 6(a-1). The increased surface roughness is likely due to the H$_2$ or O$_2$ bubbles formation during long-time stability tests [58]. Also, the formation of oxidation species such as MnO, CuOH and CuOOH leads to the modification of the crystallographic structure [59–61]. The Raman analysis before and after the stability test is shown in Fig. 6b. Less intense peaks were observed, primarily due to local crystal phase changes and the formation of an amorphous surface [62]. Further, the XRD pattern was

collected post-stability test as seen in Fig. 6c, revealing similar peaks to those of the fresh Ru/CuMnBP but with a reduced intensity. The disappearance of some sub-peaks may be attributed to the phase transformation process that can alter or diminish the crystal planes [62]. Further, the XPS characterization was conducted to investigate the chemical surface of the states of the Ru/CuMnBP electrode after stability measurement as shown in Fig. 6(d–d-4). For Ru 3d, no obvious changes were observed. In the case of Cu 2p spectrum in Fig. 6(d-2), an increase in CuO portion and peak intensity of the corresponding shakeup satellite peaks were noted, which was mainly due to the oxidation process. Similarly, for B 1s and P 2p spectra, the corresponding oxidation states are more pronounced due to the inevitable oxidation. The O 1s spectrum in Fig. S56(b) also exhibited an increased portion of oxidation states of M-O (Ru, Cu and Mn). The electrochemical performance compassion was before and after the stability test as seen in Fig. S55, indicating that the results are repeatable with minimal differences.

4. Conclusion

In summary, a novel bifunctional Ru/CuMnBP electrode was successfully fabricated for electrochemical water splitting application. The electrode required extremely low overpotentials of 11 mV for HER and 85 mV for OER at 10 mA/cm^2, facilitating efficient overall water splitting with a cell voltage of 1.53 V at 10 mA/cm^2. The superior catalytic activity of the Ru/CuMnBP electrode can be attributed to the balanced incorporation of Cu, Mn, B and P components along with Ru heteroatom doping which induced an increased number of active sites, improved conductivity and enhanced ECSA. At the industrial-level current density
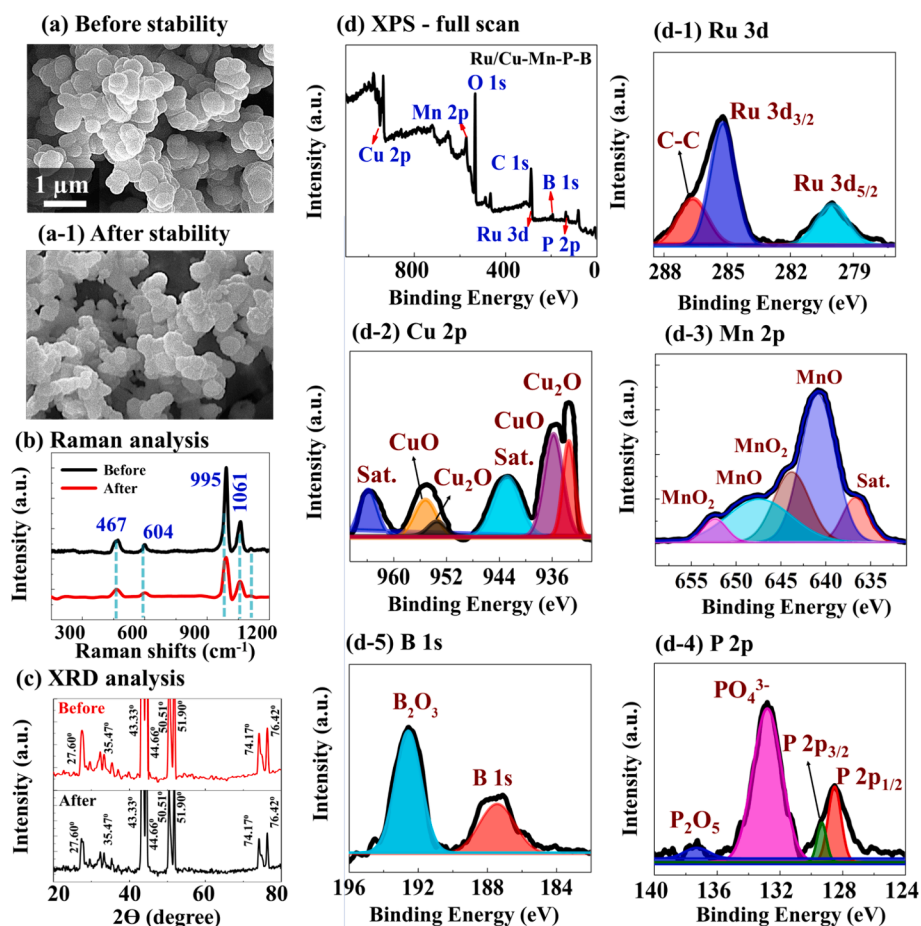

Fig. 6. Surface and elemental characterization of Ru/CuMnPB electrode after stability performance. SEM images of (a) Before and (a-1) After stability test at 1000 mA/cm^2 for 12 hrs. (b) Raman spectra comparison. (c) XRD spectra comparison. (d) Full scan of XPS spectrum of Ru/CuMnBP (anode) after the stability test. (d-1–d-5) High-resolution XPS spectra as labeled.

of 2000 mA/cm^2, the Ru/CuMnBP electrode demonstrated a cell voltage of 3.13 V, which is comparable to the benchmark system. Furthermore, the hybrid configuration of Pt/C||Ru/CuMnBP exhibited much enhanced catalyst activity, requiring only 2.64 V to maintain 2000 mA/cm^2. Also, the Ru/CuMnBP demonstrated splitting capability in acid, neutral, river water and seawater, making it a promising alternative for realistic application. Overall, our work not only offers new insights into the catalytic behavior at industrial-level current densities but also introduces a novel highly effective bi-functional electrode with high potential to replace traditional benchmark systems.

CRediT authorship contribution statement

Shusen Lin: Writing – original draft, Investigation, Data curation. **Rutuja Mandavkar:** Investigation, Data curation. **Md Ahasan Habib:** Investigation, Data curation. **Sumiya Akter Dristy:** Investigation, Data curation. **Mehedi Hasan Joni:** Investigation, Data curation. **Jae-Hun Jeong:** Supervision, Methodology, Investigation. **Jihoon Lee:** Writing – review & editing, Project administration, Funding acquisition, Conceptualization.

Declaration of competing interest

The authors declare that they have no known competing financial interests or personal relationships that could have appeared to influence the work reported in this paper.

Data availability

Data will be made available on request.

Appendix A. Supplementary data

Supplementary data to this article can be found online at https://doi.org/10.1016/j.jcis.2024.08.009.

References

[1] Z. Gao, G. Wang, T. Lei, Z. Lv, M. Xiong, L. Wang, S. Xing, J. Ma, Z. Jiang, Y. Qin, Enhanced hydrogen generation by reverse spillover effects over bicomponent catalysts, Nat. Commun. 13 (2022) 1–9.

[2] S. Guan, Y. Liu, H. Zhang, H. Wei, T. Liu, X. Wu, H. Wen, R. Shen, S. Mehdi, X. Ge, Atomic interface-exciting catalysis on cobalt nitride-oxide for accelerating hydrogen generation, Small (2022) 2107417.

[3] I. Slobodkin, E. Davydova, M. Sananis, A. Breytus, A. Rothschild, Electrochemical and chemical cycle for high-efficiency decoupled water splitting in a near-neutral electrolyte, Nat. Mater. 23 (2024) 398–405, https://doi.org/10.1038/s41563-023-01767-y.

[4] M.A. Gaikwad, V.V. Burungale, D.B. Malavekar, U.V. Ghorpade, U.P. Suryawanshi, S. Jang, X. Guo, S.W. Shin, J.-S. Ha, M.P. Suryawanshi, J.H. Kim, Self-supported Fe-based nanostructured electrocatalysts for water splitting and selective oxidation reactions: past, present, and future, Adv. Energy Mater. 14 (2024) 2303730, https://doi.org/10.1002/aenm.202303730.

[5] H. Park, J.W. Bae, T.H. Lee, I.J. Park, C. Kim, M.G. Lee, S.A. Lee, J.W. Yang, M. Choi, S.H. Hong, Surface-tailored medium entropy alloys as radically low overpotential oxygen evolution electrocatalysts, Small 18 (2022) 2105611.

[6] Y. Luo, Z. Zhang, M. Chhowalla, B. Liu, Recent advances in design of electrocatalysts for high-current-density water splitting, Adv. Mater. 34 (2022) 2108133, https://doi.org/10.1002/adma.202108133.

[7] W. He, R. Zhang, D. Cao, Y. Li, J. Zhang, Q. Hao, H. Liu, J. Zhao, H.L. Xin, Super-hydrophilic microporous Ni (OH) x/Ni3S2 heterostructure electrocatalyst for large-current-density hydrogen evolution, Small (2022) 2205719.

[8] M.N. Lakhan, A. Hanan, A.H. Shar, I. Ali, Y. Wang, M. Ahmed, U. Aftab, H. Sun, H. Arandiyan, Transition metals-based electrocatalysts for alkaline overall water splitting: advancements, challenges, and perspectives, Chem. Commun. (2024), https://doi.org/10.1039/D3CC06015B.

[9] A.S. Sabir, E. Pervaiz, R. Khosa, U. Sohail, An inclusive review and perspective on Cu-based materials for electrochemical water splitting, RSC Adv. 13 (2023) 4963–4993, https://doi.org/10.1039/D2RA07901A.

[10] A. Rajput, A. Kundu, B. Chakraborty, Recent progress on copper-based electrode materials for overall water-splitting, ChemElectroChem 8 (2021) 1698–1722.

[11] P. Wang, S. Zhang, Z. Wang, Y. Mo, X. Luo, F. Yang, M. Lv, Z. Li, X. Liu, Manganese-based oxide electrocatalysts for the oxygen evolution reaction: a review, J. Mater. Chem. A 11 (2023) 5476–5494, https://doi.org/10.1039/D2TA09039B.

[12] V.S. Kumbhar, H. Lee, J. Lee, K. Lee, Recent advances in water-splitting electrocatalysts based on manganese oxide, Carbon Resour. Convers. 2 (2019) 242–255.

[13] K. Kannimuthu, K. Sangeetha, S. Sam Sankar, A. Karmakar, R. Madhu, S. Kundu, Investigation on nanostructured Cu-based electrocatalysts for improvising water splitting: a review, Inorg. Chem. Front. 8 (2021) 234–272, https://doi.org/10.1039/D0QI01060J.

[14] Y. Zhang, C. Fu, S. Weng, H. Lv, P. Li, S. Deng, W. Hao, Construction of an "environment-friendly" CuB x@ PU self-supporting electrode toward efficient seawater electrolysis, Green Chem. 24 (2022) 5918–5929.

[15] X. Zhang, Q. Hou, S. Cao, X. Lin, X. Chen, Z. Wang, S. Wei, S. Liu, F. Dai, X. Lu, Research status, opportunities, and challenges of cobalt phosphate based materials as OER electrocatalysts, Green Chem. 25 (2023) 7883–7903, https://doi.org/10.1039/D3GC02416D.

[16] L. Wei, K. Goh, Ö. Birer, H.E. Karahan, J. Chang, S. Zhai, X. Chen, Y. Chen, A hierarchically porous nickel–copper phosphide nano-foam for efficient electrochemical splitting of water, Nanoscale 9 (2017) 4401–4408.

[17] D. Chinnadurai, M. Nallal, H. Kim, O.L. Li, K.H. Park, K. Prabakar, Mn3+ active surface site enriched manganese phosphate nano-polyhedrons for enhanced bifunctional oxygen electrocatalyst, ChemCatChem 12 (2020) 2348–2355.

[18] W. Cao, R. Zhao, G. Liu, L. Wu, J. Li, Three-dimensional ordered macroporous design of heterogeneous nickel-iron phosphide as bifunctional electrocatalyst for enhanced overall water splitting, Appl. Surf. Sci. 154905 (2022).

[19] S. Gupta, M.K. Patel, A. Miotello, N. Patel, Metal boride-based catalysts for electrochemical water-splitting: a review, Adv. Funct. Mater. 30 (2020) 1906481, https://doi.org/10.1002/adfm.201906481.

[20] Y. Yu, Q. Chen, J. Li, P. Rao, R. Li, Y. Du, C. Jia, W. Huang, J. Luo, P. Deng, Y. Shen, X. Tian, Progress in the development of heteroatom-doped nickel phosphates for electrocatalytic water splitting, J. Colloid Interface Sci. 607 (2022) 1091–1102, https://doi.org/10.1016/j.jcis.2021.09.032.

[21] C. Guo, Y. Shi, S. Lu, Y. Yu, B. Zhang, Amorphous nanomaterials in electrocatalytic water splitting, Chinese, J. Catal. 42 (2021) 1287–1296, https://doi.org/10.1016/S1872-2067(20)63740-8.

[22] S. Anantharaj, S. Noda, Amorphous catalysts and electrochemical water splitting: an untold story of harmony, Small 16 (2020) 1905779, https://doi.org/10.1002/smll.201905779.

[23] L. Tian, Z. Li, X. Xu, C. Zhang, Advances in noble metal (Ru, Rh, and Ir) doping for boosting water splitting electrocatalysis, J. Mater. Chem. A 9 (2021) 13459–13470, https://doi.org/10.1039/D1TA01108A.

[24] M. Zhao, H. Li, W. Li, J. Li, L. Yi, W. Hu, C.M. Li, Ru-doping enhanced electrocatalysis of metal-organic framework nanosheets toward overall water splitting, Chem. – A Eur. J. 26 (2020) 17091–17096, https://doi.org/10.1002/chem.202002072.

[25] X. Wang, J. Zhang, Z. Wang, Z. Lin, S. Shen, W. Zhong, Fabricating Ru single atoms and clusters on CoP for boosted hydrogen evolution reaction, Chinese J. Struct. Chem. 42 (2023) 100035, https://doi.org/10.1016/j.cjsc.2023.100035.

[26] C. Liu, L. Feng, Advances in anode catalysts of methanol-assisted water-splitting reactions for hydrogen generation, Chinese, J. Struct. Chem. (2023) 100136.

[27] H. Feizi, S.M. Hosseini, Z. Zand, M.M. Najafpour, Electrochemical induction of Mn (III) in the structure of Mn(IV) oxide: Toward a new approach for water splitting, Int. J. Hydrogen Energy. 47 (2022) 7813–7822, https://doi.org/10.1016/j.ijhydene.2021.12.127.

[28] G. Janani, S. Surendran, H. Choi, T.-Y. An, M.-K. Han, S.-J. Song, W. Park, J.K. Kim, U. Sim, Anchoring of Ni12P5 microbricks in nitrogen- and phosphorus-enriched carbon frameworks: engineering bifunctional active sites for efficient water-splitting systems, ACS Sustain. Chem. Eng. 10 (2022) 1182–1194, https://doi.org/10.1021/acssuschemeng.1c06514.

[29] Z. Wang, H. Liu, R. Ge, X. Ren, J. Ren, D. Yang, L. Zhang, X. Sun, Phosphorus-doped Co3O4 nanowire array: a highly efficient bifunctional electrocatalyst for overall water splitting, ACS Catal. 8 (2018) 2236–2241, https://doi.org/10.1021/acscatal.7b03594.

[30] L. Yang, S. Cheng, X. Ji, Y. Jiang, J. Zhou, M. Liu, Investigations into the origin of pseudocapacitive behavior of Mn3O4 electrodes using in operando Raman spectroscopy, J. Mater. Chem. A 3 (2015) 7338–7344, https://doi.org/10.1039/C5TA00223K.

[31] J. Qi, Y.-P. Lin, D. Chen, T. Zhou, W. Zhang, R. Cao, Autologous cobalt phosphates with modulated coordination sites for electrocatalytic water oxidation, Angew. Chem. Int. Ed. 59 (2020) 8917–8921, https://doi.org/10.1002/anie.202001737.

[32] T. Begildayeva, J. Theerthagiri, S.J. Lee, Y. Yu, M.Y. Choi, Unraveling the synergy of anion modulation on Co electrocatalysts by pulsed laser for water splitting: intermediate capturing by in situ/operando Raman studies, Small 18 (2022) 2204309, https://doi.org/10.1002/smll.202204309.

[33] C. Huang, B. Zhang, Y. Wu, Q. Ruan, L. Liu, J. Su, Y. Tang, R. Liu, P.K. Chu, Experimental and theoretical investigation of reconstruction and active phases on

honeycombed Ni3N-Co3N/C in water splitting, Appl. Catal. B Environ. 297 (2021) 120461, https://doi.org/10.1016/j.apcatb.2021.120461.

[34] H.-C. Chen, C.-W. Huang, J.C.S. Wu, S.-T. Lin, Theoretical investigation of the metal-doped SrTiO3 photocatalysts for water splitting, J. Phys. Chem. C 116 (2012) 7897–7903, https://doi.org/10.1021/jp300910e.

[35] N.A. Jarrah, J.G. van Ommen, L. Lefferts, Mechanistic aspects of the formation of carbon-nanofibers on the surface of Ni foam: A new microstructured catalyst support, J. Catal. 239 (2006) 460–469.

[36] Q. Luo, A.H. Jones, High-precision determination of residual stress of polycrystalline coatings using optimised XRD-sin2ψ technique, Surf. Coat. Technol. 205 (2010) 1403–1408.

[37] S. Burse, R. Kulkarni, R. Mandavkar, M.A. Habib, S. Lin, Y.-U. Chung, J.-H. Jeong, J. Lee, Vanadium-doped FeBP microsphere croissant for significantly enhanced bi-functional HER and OER electrocatalyst, Nanomaterials 12 (2022), https://doi.org/10.3390/nano12193283.

[38] R. Mandavkar, M.A. Habib, S. Lin, R. Kulkarni, S. Burse, J.-H. Jeong, J. Lee, Electron enriched ternary NiMoB electrocatalyst for improved overall water splitting: Better performance as compared to the Pt/C||RuO2 at high current density, Appl. Mater. Today. 29 (2022) 101579, https://doi.org/10.1016/j.apmt.2022.101579.

[39] Q. Wen, Y. Zhao, Y. Liu, H. Li, T. Zhai, Ultrahigh-current-density and long-term-durability electrocatalysts for water splitting, Small 18 (2022) 2104513, https://doi.org/10.1002/smll.202104513.

[40] Y. Yan, J. Huang, X. Wang, T. Gao, Y. Zhang, T. Yao, B. Song, Ruthenium incorporated cobalt phosphide nanocubes derived from a prussian blue analog for enhanced hydrogen evolution, Front. Chem. 6 (2018) 521.

[41] J. Chastain, R.C. King Jr, Handbook of X-ray photoelectron spectroscopy, Perkin-Elmer Corp. 40 (1992) 221.

[42] M. Ahasan Habib, R. Mandavkar, S. Lin, S. Burse, T. Khalid, M. Hasan Joni, J.-H. Jeong, J. Lee, Ni-B-P micro spheres for superior water splitting OER electrocatalyst satisfying industrial operational requirement, Chem. Eng. J. 462 (2023) 142177, https://doi.org/10.1016/j.cej.2023.142177.

[43] P. Wang, J. An, Z. Ye, W. Cai, X. Zheng, Cu-based multicomponent metallic compound materials as electrocatalyst for water splitting, Front. Chem. 10 (2022) 913874.

[44] A. Hameed, F. Zulfiqar, W. Iqbal, H. Ali, S.S. Ahmad Shah, M.A. Nadeem, Electrocatalytic water oxidation on CuO–Cu2O modulated cobalt-manganese layered double hydroxide, RSC Adv. 12 (2022) 28954–28960, https://doi.org/10.1039/D2RA05036F.

[45] D. Chinnadurai, A.R. Selvaraj, R. Rajendiran, G.R. Kumar, H.-J. Kim, K.K. Viswanathan, K. Prabakar, Inhibition of redox behaviors in hierarchically structured manganese cobalt phosphate supercapacitor performance by surface trivalent cations, ACS Omega 3 (2018) 1718–1725.

[46] M. Shimizu, Y. Tsushima, S. Arai, Electrochemical Na-insertion/extraction property of Ni-coated black phosphorus prepared by an electroless deposition method, ACS Omega 2 (2017) 4306–4315.

[47] W. Hao, D. Yao, Q. Xu, R. Wang, C. Zhang, Y. Guo, R. Sun, M. Huang, Z. Chen, Highly efficient overall water splitting enabled via grafting boron-inserted Fe-Ni solid solution nanosheets onto unconventional skeleton, Appl. Catal. B Environ. 292 (2021) 120188, https://doi.org/10.1016/j.apcatb.2021.120188.

[48] M. Guo, H. Meng, J. Jin, J. Mi, Amine-assisted synthesis of the Ni3Fe alloy encapsulated in nitrogen-doped carbon for high-performance water splitting, J. Mater. Chem. A 11 (2023) 6452–6464, https://doi.org/10.1039/D2TA09549A.

[49] S. Park, Y.H. Lee, S. Choi, H. Seo, M.Y. Lee, M. Balamurugan, K.T. Nam, Manganese oxide-based heterogeneous electrocatalysts for water oxidation, Energy Environ. Sci. 13 (2020) 2310–2340.

[50] T. Shinagawa, A.T. Garcia-Esparza, K. Takanabe, Insight on Tafel slopes from a microkinetic analysis of aqueous electrocatalysis for energy conversion, Sci. Rep. 5 (2015) 13801, https://doi.org/10.1038/srep13801.

[51] G. Chen, T. Wang, J. Zhang, P. Liu, H. Sun, X. Zhuang, M. Chen, X. Feng, Accelerated hydrogen evolution kinetics on NiFe-layered double hydroxide electrocatalysts by tailoring water dissociation active sites, Adv. Mater. 30 (2018) 1706279.

[52] M.A. Habib, S. Burse, S. Lin, R. Mandavkar, M.H. Joni, J.-H. Jeong, S.-S. Lee, J. Lee, Dual-functional Ru/Ni-B-P electrocatalyst toward accelerated water electrolysis and high-stability, Small 20 (2024) 2307533, https://doi.org/10.1002/smll.202307533.

[53] R. Dai, H. Liu, X. Zhi, S. Di, B. Zhai, J. He, P. Niu, S. Wang, L. Li, A composite acidic electrolyte for ultra-long-life hydrogen-ion storage, Chem. Eng. J. 448 (2022) 137655.

[54] J. Wang, Z. Wei, S. Mao, H. Li, Y. Wang, Highly uniform Ru nanoparticles over N-doped carbon: pH and temperature-universal hydrogen release from water reduction, Energy Environ. Sci. 11 (2018) 800–806.

[55] S. Anantharaj, S. Kundu, S. Noda, Worrisome exaggeration of activity of electrocatalysts destined for steady-state water electrolysis by polarization curves from transient techniques, J. Electrochem. Soc. 169 (2022) 14508, https://doi.org/10.1149/1945-7111/ac47ec.

[56] K. Izumiya, E. Akiyama, H. Habazaki, N. Kumagai, A. Kawashima, K. Hashimoto, Effects of additional elements on electrocatalytic properties of thermally decomposed manganese oxide electrodes for oxygen evolution from seawater, Mater. Trans. JIM. 38 (1997) 899–905.

[57] S.J. Patil, N.R. Chodankar, S.-K. Hwang, P.A. Shinde, G.S.R. Raju, K.S. Ranjith, Y.S. Huh, Y.-K. Han, Co-metal–organic framework derived CoSe2@ MoSe2 core–shell structure on carbon cloth as an efficient bifunctional catalyst for overall water splitting, Chem. Eng. J. 429 (2022) 132379.

[58] S.M. Taylor, A. Pătru, D. Perego, E. Fabbri, T.J. Schmidt, Influence of carbon material properties on activity and stability of the negative electrode in vanadium redox flow batteries: a model electrode study, ACS Appl. Energy Mater. 1 (2018) 1166–1174.

[59] M.A. Ashraf, C. Li, B.T. Pham, D. Zhang, Electrodeposition of Ni–Fe–Mn ternary nanosheets as affordable and efficient electrocatalyst for both hydrogen and oxygen evolution reactions, Int. J. Hydrogen Energy. 45 (2020) 24670–24683, https://doi.org/10.1016/j.ijhydene.2020.06.249.

[60] P. Plate, C. Höhn, U. Bloeck, P. Bogdanoff, S. Fiechter, F.F. Abdi, R. van de Krol, A.C. Bronneberg, On the origin of the OER activity of ultrathin manganese oxide films, ACS Appl. Mater. Interfaces. 13 (2021) 2428–2436.

[61] M. Sajid, W. Qayyum, A. Farhan, M.A. Qamar, H. Nawaz, Progress in the development of copper oxide-based materials for electrochemical water splitting, Int. J. Hydrogen Energy. 62 (2024) 209–227, https://doi.org/10.1016/j.ijhydene.2024.02.377.

[62] Z. Fahimi, O. Moradlou, A. Sabbah, K.-H. Chen, L.-C. Chen, M. Qorbani, Co3V2O8 hollow spheres with mesoporous walls as high-capacitance electrode for hybrid supercapacitor device, Chem. Eng. J. 436 (2022) 135225.

[63] A.M. Harzandi, S. Shadman, M. Ha, C.W. Myung, D.Y. Kim, H.J. Park, S. Sultan, W.-S. Noh, W. Lee, P. Thangavel, Immiscible bi-metal single-atoms driven synthesis of electrocatalysts having superb mass-activity and durability, Appl. Catal. B Environ. 270 (2020) 118896.

[64] Y. Chen, Y. Zhang, X. Zhang, T. Tang, H. Luo, S. Niu, Z. Dai, L. Wan, J. Hu, Self-templated fabrication of MoNi4/MoO3-x nanorod arrays with dual active components for highly efficient hydrogen evolution, Adv. Mater. 29 (2017) 1703311.

[65] W. Dai, L. Lin, Y. Li, Z. Chen, F. Liu, F. Li, L. Chen, A novel Ni-S-Mn electrode with hierarchical morphology fabricated by gradient electrodeposition for hydrogen evolution reaction, Appl. Surf. Sci. 514 (2020) 145944.

[66] M.A. Habib, R. Mandavkar, S. Burse, S. Lin, R. Kulkarni, C.S. Patil, J.-H. Jeong, J. Lee, Design of boron-based ternary W3CoB3 electrocatalyst for the improved HER and OER performances, Mater. Today Energy (2022) 101021, https://doi.org/10.1016/j.mtener.2022.101021.

[67] C. Tang, L. Gan, R. Zhang, W. Lu, X. Jiang, A.M. Asiri, X. Sun, J. Wang, L. Chen, Ternary FexCo1−xP nanowire array as a robust hydrogen evolution reaction electrocatalyst with Pt-like activity: experimental and theoretical insight, Nano Lett. 16 (2016) 6617–6621, https://doi.org/10.1021/acs.nanolett.6b03332.

[68] J. Tian, Q. Liu, A.M. Asiri, X. Sun, Self-supported nanoporous cobalt phosphide nanowire arrays: an efficient 3D hydrogen-evolving cathode over the wide range of pH 0–14, J. Am. Chem. Soc. 136 (2014) 7587–7590, https://doi.org/10.1021/ja503372r.

[69] S. Lin, M.A. Habib, R. Mandavkar, R. Kulkarni, S. Burse, Y. Chung, C. Liu, Z. Wang, S. Lin, J. Jeong, Higher water-splitting performance of boron-based porous CoMnB electrocatalyst over the benchmarks at high current in 1 m KOH and real sea water, Adv. Sustain. Syst. (2022) 2200213.

[70] J. Zhuo, M. Cabán-Acevedo, H. Liang, L. Samad, Q. Ding, Y. Fu, M. Li, S. Jin, High-performance electrocatalysis for hydrogen evolution reaction using Se-doped pyrite-phase nickel diphosphide nanostructures, ACS Catal. 5 (2015) 6355–6361.

[71] Y. Zhang, Y. Liu, M. Ma, X. Ren, Z. Liu, G. Du, A.M. Asiri, X. Sun, A Mn-doped Ni2P nanosheet array: An efficient and durable hydrogen evolution reaction electrocatalyst in alkaline media, Chem. Commun. 53 (2017) 11048–11051, https://doi.org/10.1039/c7cc06278h.

[72] M. Cao, Z. Xue, J. Niu, J. Qin, M. Sawangphruk, X. Zhang, R. Liu, Facile electrodeposition of Ni–Cu–P dendrite nanotube films with enhanced hydrogen evolution reaction activity and durability, ACS Appl. Mater. Interfaces. 10 (2018) 35224–35233.

[73] Y.S. Park, W.-S. Choi, M.J. Jang, J.H. Lee, S. Park, H. Jin, M.H. Seo, K.-H. Lee, Y. Yin, Y. Kim, Three-dimensional dendritic Cu–Co–P electrode by one-step electrodeposition on a hydrogen bubble template for hydrogen evolution reaction, ACS Sustain. Chem. Eng. 7 (2019) 10734–10741.

[74] J. Tian, Q. Liu, N. Cheng, A.M. Asiri, X. Sun, Self-supported Cu3P nanowire arrays as an integrated high-performance three-dimensional cathode for generating hydrogen from water, Angew. Chem. 126 (2014) 9731–9735.

[75] S. Wei, K. Qi, Z. Jin, J. Cao, W. Zheng, H. Chen, X. Cui, One-step synthesis of a self-supported copper phosphide nanobush for overall water splitting, ACS Omega 1 (2016) 1367–1373.

[76] Y. Liu, J. Cao, Y. Chen, M. Wei, X. Liu, X. Li, Q. Wu, B. Feng, Y. Zhang, L. Yang, Regulation of the morphology and electrochemical properties of Ni0.85Se via Fe doping for overall water splitting and supercapacitors, CrstEngComm 24 (2022) 1704–1718, https://doi.org/10.1039/D1CE01555A.

[77] A. Sivanantham, P. Ganesan, S. Shanmugam, Hierarchical NiCo2S4 nanowire arrays supported on Ni foam: an efficient and durable bifunctional electrocatalyst for oxygen and hydrogen evolution reactions, Adv. Funct. Mater. 26 (2016) 4661–4672, https://doi.org/10.1002/adfm.201600566.

[78] H. Hosseini, M. Roushani, Rational design of hollow core-double shells hybrid nanoboxes and nanopipes composed of hierarchical Cu-Ni-Co selenides anchored on nitrogen-doped carbon skeletons as efficient and stable bifunctional electrocatalysts for overall water splitting, Chem. Eng. J. 402 (2020) 126174.

[79] Y. Rong, Y. Ma, F. Guo, J. Qian, H. Li, M. Zhou, Z. Xu, Y.-Q. Zheng, T.-T. Li, Paintbrush-like Co doped Cu3P grown on Cu foam as an efficient janus electrode for overall water splitting, Int. J. Hydrogen Energy. 44 (2019) 28833–28840.

[80] Y. Gong, Y. Zhi, Y. Lin, T. Zhou, J. Li, F. Jiao, W. Wang, Controlled synthesis of bifunctional particle-like Mo/Mn-Ni x S y/NF electrocatalyst for highly efficient overall water splitting, Dalt. Trans. 48 (2019) 6718–6729.

[81] C. Dong, T. Kou, H. Gao, Z. Peng, Z. Zhang, Eutectic-derived mesoporous Ni-Fe-O nanowire network catalyzing oxygen evolution and overall water splitting, Adv. Energy Mater. 8 (2018) 1701347.

[82] D. Wang, J. Li, Y. Zhao, H. Xu, J. Zhao, Bifunctional Cu2S–Co (OH) 2 nanotube array/Cu foam electrocatalyst for overall water splitting, Electrochim. Acta. 316 (2019) 8–18.

[83] A.I. Inamdar, H.S. Chavan, B. Hou, C.H. Lee, S.U. Lee, S. Cha, H. Kim, H. Im, A robust nonprecious CuFe composite as a highly efficient bifunctional catalyst for overall electrochemical water splitting, Small 16 (2020) 1905884.

[84] Z. Ma, X. Gu, G. Liu, Q. Zhao, J. Li, X. Wang, Bimetallic Cu–Co–Se nanotube arrays assembled on 3D framework: an efficient bifunctional electrocatalyst for overall water splitting, ChemSusChem 14 (2021) 5065–5074.

[85] N. Xu, G. Cao, Z. Chen, Q. Kang, H. Dai, P. Wang, Cobalt nickel boride as an active electrocatalyst for water splitting, J. Mater. Chem. A 5 (2017) 12379–12384, https://doi.org/10.1039/c7ta02644g.